Available online at www.sciencedirect.com
ScienceDirect
Journal of Computational Physics 222 (2007) 391–407
JOURNAL OF COMPUTATIONAL PHYSICS
www.elsevier.com/locate/jcp

A high-order discontinuous Galerkin method for the unsteady incompressible Navier–Stokes equations

Khosro Shahbazi [a,*], Paul F. Fischer [b], C. Ross Ethier [a]

[a] *University of Toronto, Department of Mechanical and Industrial Engineering, 5 King's College Road, Toronto, Ont., Canada M5S 3G8*
[b] *Argonne National Laboratory, 9700 S. Case Avenue, Argonne, IL 60439, USA*

Received 15 February 2006; received in revised form 15 June 2006; accepted 25 July 2006
Available online 18 September 2006

Abstract

We present a high-order discontinuous Galerkin discretization of the unsteady incompressible Navier–Stokes equations in convection-dominated flows using triangular and tetrahedral meshes. The scheme is based on a semi-explicit temporal discretization with explicit treatment of the nonlinear term and implicit treatment of the Stokes operator. The nonlinear term is discretized in divergence form by using the local Lax–Friedrichs fluxes; thus, local conservativity is inherent. Spatial discretization of the Stokes operator has employed both equal-order ($P_k - P_k$) and mixed-order ($P_k - P_{k-1}$) velocity and pressure approximations. A second-order approximate algebraic splitting is used to decouple the velocity and pressure calculations leading to an algebraic Helmholtz equation for each component of the velocity and a consistent Poisson equation for the pressure. The consistent Poisson operator is replaced by an equivalent (in stability and convergence) operator, namely that arising from the interior penalty discretization of the standard Poisson operator with appropriate boundary conditions. This yields a simpler and more efficient method, characterized by a compact stencil size.

We show the temporal and spatial behavior of the method by solving some popular benchmarking tests. For an unsteady Stokes problem, second-order temporal convergence is obtained, while for the Taylor vortex test problem on both semi-structured and fully unstructured triangular meshes, spectral convergence with respect to the polynomial degree k is obtained. By studying the Orr–Sommerfeld stability problem, we demonstrate that the $P_k - P_k$ method yields a stable solution, while the $P_k - P_{k-1}$ formulation leads to unphysical instability. The good performance of the method is further shown by simulating vortex shedding in flow past a square cylinder. We conclude that the proposed discontinuous Galerkin method with the $P_k - P_k$ formulation is an efficient scheme for accurate and stable solution of the unsteady Navier–Stokes equations in convection-dominated flows.

Keywords: Discontinuous Galerkin methods; High-order methods; Navier–Stokes equations; Incompressible flows; Algebraic splitting methods

* Corresponding author. Tel.: +1 4166040868; fax: +1 4169787753.
E-mail addresses: shahbazi@mie.utoronto.ca (K. Shahbazi), fischer@mcs.anl.gov (P.F. Fischer), ethier@mie.utoronto.ca (C.R. Ethier).

0021-9991/$ - see front matter
doi:10.1016/j.jcp.2006.07.029

1. Introduction

Discontinuous Galerkin (DG) methods are gaining popularity in solving partial differential equations arising from modeling diverse scientific and engineering problems. Compared with the classical continuous Galerkin methods, DG methods have advantages in facilitating non-conforming mesh and functional adaptivity, retaining the local conservativity of physical quantities and yielding more robust discretizations in high Reynolds number flow simulations (e.g., [19,24,26]).

DG methods for pure elliptic problems and hyperbolic conservation laws have been extensively developed and analyzed during the past three decades (e.g, see the review articles [2] for elliptic problems and [24] for hyperbolic systems). Only recently, however have the DG methods been extended to the numerical solution of incompressible flows, including the Stokes and the incompressible Navier–Stokes equations (see articles [20,18,21] for the Stokes problem and [29,23] for the Navier–Stokes equations). All of the above work has considered only stationary Stokes or Navier–Stokes equations. Therefore, the objective of this paper is to propose an efficient DG scheme for the unsteady incompressible Navier–Stokes equations. Our approach is tailored to convection-dominated regimes encountered in transitional and turbulent flows. The approach is based on a semi-explicit temporal discretization in which the convective term is treated explicitly and the Stokes operator is treated implicitly. It employs a high-order DG spatial discretization on triangular and tetrahedral elements in two and three space dimensions, respectively. To put our methodology in perspective, we review related work on the DG treatment of the convective and Stokes operators.

1.1. Review of DG discretization of the convective operator

Several DG methods for the spatial discretization of the convective term have recently been proposed. Cockburn et al. [22] provided an a priori error estimate for the DG solution of the Oseen problem by treating the linear convective term with an upwinding scheme. For the nonlinear Navier–Stokes equations with non-overlapping domain decompositions, Girault et al. [29] devised a stable method by discretizing the convective term in a skew-symmetric form. To assure that the DG formulation yields a locally conservative discretization, a property that is not offered by the above two methods, Cockburn et al. [23] proposed two strategies. In the first, they linearized the convective term and then used the results of [22] for the Oseen problem to prove the stability of the discrete solution. Through an iterative procedure they then recovered a locally conservative velocity field. In their second formulation, the pressure p was replaced with the Bernoulli pressure $p + \frac{1}{2}|\mathbf{u}|^2$; hence, local conservativity was attained. With this method, one can prove the boundedness of the approximate solution for the case of Dirichlet boundary conditions. For the case of outflow boundary conditions, however, this type of formulation leads to an unphysical solution at the outlet, as previously shown in the context of the continuous Galerkin approximation [12]. Thus, for engineering problems that are typically formulated on truncated domains with outflow boundary conditions, this method is not suitable.

We here propose a new strategy. We discretize the nonlinear term in the divergence form and use the local Lax–Friedrichs numerical fluxes to obtain stable results. Discretizing the nonlinear term in the divergence form immediately yields local conservativity, a property that the two previously proposed methods either do not offer (the method of Girault et al. [29]) or require an extra iteration procedures to attain (the first method of Cockburn et al. [23]). Unlike the second method of Cockburn et al. [23], our method applies to any boundary conditions, including Dirichlet, periodic, and outflow conditions.

1.2. Review of DG discretization of the Stokes operator

For the DG discretization of the Stokes operator, several studies have been reported in the literature, beginning with Hansbo and Larson [20]. For simplicial triangulations, they used the interior penalty (IP) method [1] for the viscous term and approximating polynomial degrees k and $k-1$ for the velocity and the pressure, respectively ($P_k - P_{k-1}$, mixed-order formulation). Cockburn et al. [21] used the so-called local DG method for the viscous term [32,25] and proved an inf-sup condition for equal approximating polynomial degree, k for the velocity and pressure ($P_k - P_k$, equal-order formulation), by adding a stabilization term to the discretized divergence-free constraint. Schötzau et al. [19] similarly employed the equal-order formulation but with an IP

discretization of the Laplacian. In our methodology, we consider the IP method for the viscous term and both the $P_k - P_{k-1}$ and $P_k - P_k$ formulations. We prefer the IP method over the local DG method for its simplicity and its compact stencil size.

Employing the semi-explicit temporal and the DG spatial discretizations leads to an algebraic Stokes system to solve at each time step. For this system, we propose a new class of second-order approximate splitting methods. Applying algebraic splitting procedures introduced earlier in the context of the finite volume, finite element or spectral element methods (e.g., [38,30,5], respectively) yields a Helmholtz system for the velocity and a consistent Poisson equation with an extended stencil size for the pressure variable to be solved at each time step. In the DG setting, however, we are able to replace this pressure operator with an equivalent operator that is simpler and computationally more efficient. This operator offers a compact stencil size and arises from the IP discretization of the Poisson equation with appropriate boundary conditions.

We note that the application of the algebraic splitting for solving the Stokes system on triangular or tetrahedral meshes is more advantageous in the DG setting than in the continuous Galerkin method. In the DG setting, the pressure operator has compact stencil-size, and the mass matrix is block diagonal. The block diagonal structure of the mass matrix permits a simple and efficient preconditioner for the iterative solution of the Helmholtz system of the velocity as explained in Section 2. None of these properties exists in the continuous counterpart. Furthermore, our algebraic splitting approach is superior to the Chorin–Temam projection scheme (differential splittings) [43,44] in the sense that our scheme avoids unphysical boundary conditions for the pressure equation inherent in the differential splittings.

Below, we describe details of our solution procedure. We then present some implementation details in Section 3. These are followed in Section 4 by numerical experiments to demonstrate the temporal and spatial accuracy of the method. In Section 5, the work is summarized and some future directions are explored.

2. Navier–Stokes discretization

We seek the numerical solution of the unsteady incompressible Navier–Stokes equations

$$\frac{\partial \mathbf{u}}{\partial t} + \mathbf{u}\cdot\nabla\mathbf{u} = \frac{1}{Re}\nabla^2\mathbf{u} - \nabla p + \mathbf{f} \quad \text{in } \Omega\times[0,T], \tag{1a}$$

$$\nabla\cdot\mathbf{u} = 0 \quad \text{in } \Omega\times[0,T], \tag{1b}$$

$$\mathbf{u}(t=0) = \mathbf{u}_0 \quad \text{in } \Omega, \tag{1c}$$

$$\mathbf{u} = \mathbf{g}_{\mathrm{D}} \quad \text{on } \partial\Omega_{\mathrm{D}}, \tag{1d}$$

$$\frac{1}{Re}\frac{\partial \mathbf{u}}{\partial n} - p\mathbf{n} = 0 \quad \text{on } \partial\Omega_N, \tag{1e}$$

$$s(\mathbf{x}) = s(\mathbf{x}') \quad \mathbf{x},\mathbf{x}'\in\partial\Omega_P, \tag{1f}$$

where $\mathbf{u}$ and p are the non-dimensionalized velocity vector and pressure, respectively, and $\mathbf{f}$ is a known body force. The Reynolds number is $Re = (UL)/\nu$, with U a characteristic velocity, L a length scale, t a dimensionless time and ν the kinematic viscosity. Eq. (1c) represents an appropriate initial condition, and Eqs. (1d)–(1f) represent Dirichlet, outflow, and periodic boundary conditions (BCs), respectively. Note that $\partial\Omega = \partial\Omega_{\mathrm{D}}\cup\partial\Omega_N\cup\partial\Omega_P$. s represents any component of the velocity vector or the pressure, and $\mathbf{x}$ and $\mathbf{x}'$ are two periodic points. Ω is a polygonal domain of dimension $d = 2$, or 3, and T is the total integration time.

The numerical solution of the above system consists of two parts: temporal discretization and spatial discretization. For temporal discretization, we use a semi-explicit scheme, in which the nonlinear term is treated explicitly and the Stokes operator is treated implicitly. We use a third-order backward differentiation (BD3) scheme for the unsteady term and a third-order extrapolation (EX3) for the nonlinear term, as proposed by Karniadakis et al. [13]. Let the total integration time T be divided into uniform time steps of size Δt. Then the semi-discretized forms of Eqs. (1a) and (1b) at time step n become

$$\left(-\frac{1}{Re}\nabla^2 + \frac{\beta_0}{\Delta t}\right)\mathbf{u}^{n+1} + \nabla p^{n+1} = \left(\frac{\beta_1}{\Delta t}\mathbf{u}_1^n + \frac{\beta_2}{\Delta t}\mathbf{u}_2^{n-1} + \frac{\beta_3}{\Delta t}\mathbf{u}_2^{n-2}\right) - (\gamma_1\mathbf{c}^n + \gamma_2\mathbf{c}^{n-1} + \gamma_3\mathbf{c}^{n-2}) + \mathbf{f}^{n+1} \quad \text{in } \Omega, \tag{2a}$$

$$\nabla\cdot\mathbf{u}^{n+1} = 0 \quad \text{in } \Omega. \tag{2b}$$

Here **c** represents the nonlinear term; $\beta_0 = 11/6$, $\beta_1 = 3$, $\beta_2 = -3/2$, and $\beta_3 = 1/3$ are coefficients associated with BD3; and $\gamma_1 = 3$, $\gamma_2 = -3$, and $\gamma_3 = 1$ are coefficients associated with EX3. For ease of notation, we will drop the superscripts referring to the time steps and absorb the right-hand side of Eq. (2a) into **f**.

Due to the explicit treatment of the convective term, time steps are limited by a CFL condition. We choose Δt based on the estimate

$$\Delta t \approx \mathcal{O}\left(\frac{\mathscr{L}}{\mathscr{U}k^2}\right), \tag{3}$$

reported in [14] for an advection model problem. Here $\mathscr{L}$ is an integral length scale (typically the mesh element size) and $\mathscr{U}$ is a characteristic velocity.

Below, we introduce some notation and approximate spaces, then describe the spatial discretization including the DG treatment of the nonlinear and Stokes operators.

2.1. Preliminaries

Let Γ_{I} denote the collection of all interior faces[1]. Then $\Gamma_{\mathrm{IDP}} = \Gamma_{\mathrm{I}} \cup \partial\Omega_{\mathrm{D}} \cup \partial\Omega_{\mathrm{P}}$, $\Gamma_{\mathrm{INP}} = \Gamma_{\mathrm{I}} \cup \partial\Omega_{\mathrm{N}} \cup \partial\Omega_{\mathrm{P}}$, and $\Gamma_{\mathrm{IDNP}} = \Gamma_{\mathrm{I}} \cup \partial\Omega_{\mathrm{D}} \cup \partial\Omega_{\mathrm{N}} \cup \partial\Omega_{\mathrm{P}}$. On a face $e \in \Gamma_{\mathrm{I}}$ shared with two elements K^+ and K^-, we permanently associate e with a unit normal vector $\mathbf{n}_e$ directed from K^+ to K^-, and define the jump and average operators of a function ϕ by

$$[\![\phi]\!] := (\phi|_{K^+})|_e - (\phi|_{K^-})|_e, \quad \{\phi\} = \frac{1}{2}(\phi|_{K^+})|_e + \frac{1}{2}(\phi|_{K^-})|_e.$$

For $e \in \partial\Omega_P$, we use the same definitions except that if K^+ contains e, K^- is an element containing the periodic face of e. On a Dirichlet or outflow face e, $\mathbf{n}_e$ is the unit normal vector $\mathbf{n}$ outward to Ω, and the jump and average of the operator ϕ coincide with the trace of ϕ.

The discontinuous approximate spaces we use are

$$\mathscr{V}_k := \{v \in L^2(\Omega) | v|_K \in P_k(K), \quad \forall K \in \mathscr{T}_h\} \tag{4}$$

and its vector version $\mathscr{V}_k^d$. $P_k(K)$ is the set of polynomials of total degree at most k on K, $k \geqslant 1$, with K being a simplicial element of the geometrically conforming triangulation $\mathscr{T}_h$ of the domain Ω. While our methodology applies to a geometrically and functionally nonconforming approximation, for simplicity, we consider only conforming triangulations and uniform polynomial degrees over all elements.

2.2. Nonlinear treatment

Using the divergence free constraint $\nabla \cdot \mathbf{u} = 0$, we write the nonlinear term in the divergence form

$$\mathbf{u} \cdot \nabla \mathbf{u} = \mathbf{u} \cdot \nabla \mathbf{u} + \mathbf{u} \nabla \cdot \mathbf{u} \equiv \nabla \cdot (\mathbf{u} \otimes \mathbf{u}),$$

where $\mathbf{u} \otimes \mathbf{v} := u_i v_j$, $i, j = 1, \ldots, d$. We can now use ideas for the DG discretization of the nonlinear term previously developed in the context of hyperbolic conservation laws [24]. Let $\mathbf{u}$ be approximated by $\mathbf{u}_h \in \mathscr{V}_k^d$; for simplicity we use $\underline{\underline{g}}$ instead of $\mathbf{u}_h \otimes \mathbf{u}_h$ hereafter. Multiplying the nonlinear term by a test function $\mathbf{v}_h \in \mathscr{V}_k^d$, integrating over the whole domain Ω, and carrying out integration by parts, we obtain

$$\int_\Omega \mathbf{v}_h \cdot \nabla \cdot \underline{\underline{g}} \, \mathrm{d}\mathbf{x} = -\sum_K \int_K \underline{\underline{g}} \cdot \nabla \cdot \mathbf{v}_h \, \mathrm{d}\mathbf{x} + \sum_{\Gamma_{\mathrm{IDNP}}} \int_e \mathbf{n}_e \cdot [\![\underline{\underline{g}} \cdot \mathbf{v}_h]\!] \, \mathrm{d}s.$$

To complete the discretization, we replace the integrand $\mathbf{n}_e \cdot [\![\underline{\underline{g}} \cdot \mathbf{v}_h]\!]$ in the surface integral with the local Lax–Friedrich fluxes $\widehat{\mathbf{n}_e \cdot [\![\underline{\underline{g}} \cdot \mathbf{v}_h]\!]}$

$$\int_\Omega \mathbf{v}_h \cdot \nabla \cdot \underline{\underline{g}} \, \mathrm{d}\mathbf{x} = -\sum_K \int_K \underline{\underline{g}} \cdot \nabla \cdot \mathbf{v}_h \, \mathrm{d}\mathbf{x} + \sum_{\Gamma_{\mathrm{IDNP}}} \int_e \widehat{\mathbf{n}_e \cdot [\![\underline{\underline{g}} \cdot \mathbf{v}_h]\!]} \, \mathrm{d}s, \tag{5}$$

[1] The terms "face" and "surface integral" denote edge and line integral in two space dimensions as well.

where

$$\overbrace{\mathbf{n}_e \cdot [\![\underline{\underline{g}} \cdot \mathbf{v}_h]\!]} = \mathbf{n}_e \cdot \{\underline{\underline{g}}\} \cdot [\![\mathbf{v}_h]\!] + \frac{1}{2} \Lambda_{K,e} [\![\mathbf{u}_h]\!] \cdot [\![\mathbf{v}_h]\!]. \tag{6}$$

In Eq. (6), and only in Eq. (6), and for $e \in \Omega_D$, the operators $\{\}$ and $[\![]\!]$ have slightly different interpretations than those previously defined. Specifically, for $e \in \Omega_D$, $\{\underline{\underline{g}}\} = \frac{1}{2}((\mathbf{u}_h \otimes \mathbf{u}_h)|_e + (\mathbf{g}_D \otimes \mathbf{g}_D)|_e)$ and $[\![\mathbf{u}_h]\!] = (\mathbf{u}_h|_e - \mathbf{g}_D|_e)$. To define $\Lambda_{K,e}$, let λ^+ and λ^- be the largest eigenvalue (in absolute value) of the Jacobians $(\partial/\partial \mathbf{u})(\underline{\underline{g}} \cdot \mathbf{n}_e)|_{\bar{\mathbf{u}}_{K^+}}$ and $(\partial/\partial \mathbf{u})(\underline{\underline{g}} \cdot \mathbf{n}_e)|_{\bar{\mathbf{u}}_{K^-}}$, respectively, with $\bar{\mathbf{u}}_{K^+}$ and $\bar{\mathbf{u}}_{K^-}$ being the mean values of $\mathbf{u}_h$ over the entire element K^+ and K^-, respectively. Then,

$$\Lambda_{K,e} = \max(\lambda^+, \lambda^-). \tag{7}$$

For $e \in \Omega_P$ and $e \in \Omega_D$, $\Lambda_{K,e}$ is defined similarly. Specifically, for $e \in \Omega_P$ and K^+ containing e, K^- contains the periodic face of e. For $e \in \Omega_D$ and $\bar{\mathbf{u}}_{K^+}$ being the mean of $\mathbf{u}_h$ on K^+ containing e, $\bar{\mathbf{u}}_{K^-} = \mathbf{g}_D$. For $e \in \Omega_N$, $\Lambda_{K,e} = 0$.

Remark 1. The terms $\underline{\underline{g}} \cdot \nabla \cdot \mathbf{v}_h$ and $\mathbf{n}_e \cdot \{\underline{\underline{g}}\} \cdot [\![\mathbf{v}_h]\!]$ in Eqs. (5) and (6) are evaluated in index notation as:

$$\underline{\underline{g}} \cdot \nabla \cdot \mathbf{v}_h := g_{ij} \frac{\partial v_{hi}}{\partial x_j}, \quad i,j = 1, \ldots, d, \tag{8a}$$

$$\mathbf{n}_e \cdot \{\underline{\underline{g}}\} \cdot [\![\mathbf{v}_h]\!] := n_{ej} \{g_{ij}\} [\![v_{hi}]\!], \quad i,j = 1, \ldots, d, \tag{8b}$$

where repeated indices imply summation.

Remark 2. This choice of the numerical fluxes leads to a compact stencil size. As shown in Fig. 1a, the degrees of freedom (DOF) of a reference element (black triangle) couple only with those of its immediate neighbors (dark grey triangles).

2.3. Stokes discretization

To set the stage for describing our solution procedure for the unsteady Stokes system (2), we first review two DG discretizations of the Poisson problem: the IP method of Arnold [1] and the method of Bassi and Rebay [32], further developed in [25]. The latter method is referred to as the local DG method.

We seek the IP and the local DG formulations of the Poisson equation with Dirichlet, Neumann, and periodic boundary conditions:

$$-\Delta u = f \quad \text{in } \Omega, \tag{9a}$$

$$u = g_D \quad \text{on } \partial\Omega_D, \tag{9b}$$

$$\nabla u \cdot \mathbf{n} = g_N, \quad \text{on } \partial\Omega_N, \tag{9c}$$

$$u(\mathbf{x}) = u(\mathbf{x}') \quad \mathbf{x}, \mathbf{x}' \in \partial\Omega_P. \tag{9d}$$

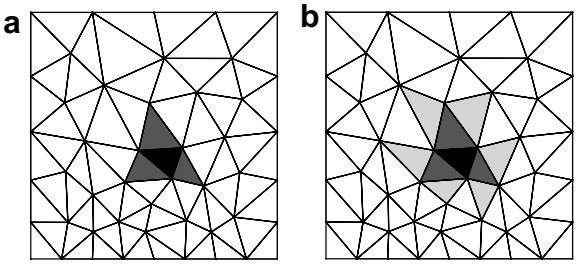

Fig. 1. (a) Compact stencil of the IP discretization of the Laplacian, and the DG treatment of the nonlinear term discussed in Section 2.2 on an unstructured triangular mesh (DOF of the black triangle couple with those of dark grey triangles); (b) the extended stencil size of the local DG discretization of the Laplacian on the same mesh (DOF of the black triangle couple with those of dark grey as well as light grey triangles). The reference triangle is shown in black, the immediate neighbors of the reference triangle are denoted in dark grey, and the second layer of the neighbors is in light grey.

2.3.1. IP formulation of the Poisson equation

In the IP formulation, the discontinuous approximation to the exact solution u, u_h, is a member of the finite element space $\mathscr{V}_k$. The approximate solution is defined by requiring that

$$a_h(u_h, v_h) = f_h(v_h) \quad \forall v_h \in \mathscr{V}_k,$$

where

$$a_h(u,v) = \sum_K \int_K \nabla u \cdot \nabla v \, \mathrm{d}\mathbf{x} - \sum_{\Gamma_{\mathrm{IDP}}} \int_e [\mathbf{n}_e \cdot \{\nabla u\}[\![v]\!] + \mathbf{n}_e \cdot \{\nabla v\}[\![u]\!]] \, \mathrm{d}s + \sum_{\Gamma_{\mathrm{IDP}}} \int_e \mu [\![u]\!][\![v]\!] \, \mathrm{d}s, \tag{10a}$$

$$f_h(v) = \int_\Omega f v \, \mathrm{d}\mathbf{x} + \int_{\partial\Omega_{\mathrm{N}}} g_{\mathrm{N}} v \, \mathrm{d}s + \int_{\partial\Omega_{\mathrm{D}}} g_{\mathrm{D}} (\mu v - \nabla v \cdot \mathbf{n}) \, \mathrm{d}s. \tag{10b}$$

The last term in Eq. (10a) is called the penalty term. It is added to enforce the coercivity of the bilinear form, which requires the choice of a sufficiently large value for the penalty parameter μ. The last integral in Eq. (10b) is due to the weak imposition of the Dirichlet boundary conditions.

The minimum acceptable value for μ depends on the triangulation and the approximating polynomial degree. Although an explicit expression for μ is not known for a general mesh topology, an expression for the case of simplicial elements has been recently derived [31]. Specifically, here we have used

$$\mu = \frac{(k+1)(k+d)}{d} \max_K \left(\frac{S_K}{V_K} \right), \tag{11}$$

where S_K and V_K represent the surface area (perimeter in two dimensions) and volume (area in two dimensions) of the element K, respectively. This is a slightly simplified version of Eq. (8) in [31].

2.3.2. Local DG formulation of the Poisson equation

In the local DG method, the Laplacian is first written as two first-order operators by introducing the auxiliary variable $\boldsymbol{\sigma}$:

$$\nabla u = \boldsymbol{\sigma}, \tag{12a}$$

$$-\nabla \cdot \boldsymbol{\sigma} = f. \tag{12b}$$

In previous work, the approximations to u and $\boldsymbol{\sigma}$, u_h and $\boldsymbol{\sigma}_h$, have belonged to $\mathscr{V}_k$ and $\mathscr{V}_k^d$, that is, spaces with equal polynomial degrees (equal-order method). In addition to the equal polynomial degree spaces, here we allow $u_h \in \mathscr{V}_k$ and $\boldsymbol{\sigma}_h \in \mathscr{V}_{k+1}^d$, spaces with mixed polynomial degrees (mixed-order method). This approach is similar to our DG method for the Stokes operator, where both equal- and mixed-order methods are allowed.

The approximate solutions u_h and $\boldsymbol{\sigma}_h$ are then defined by requiring that

$$d_h(\boldsymbol{\tau}_h, u_h) = b_h(\boldsymbol{\sigma}_h, \boldsymbol{\tau}_h) + g_h(\boldsymbol{\tau}_h) \quad \forall \boldsymbol{\tau}_h \in \mathscr{V}_k^d / \mathscr{V}_{k+1}^d, \tag{13a}$$

$$-d_h(\boldsymbol{\sigma}_h, v_h) + e_h(u_h, v_h) = f_h(v_h) \quad \forall v_h \in \mathscr{V}_k, \tag{13b}$$

where

$$d_h(\boldsymbol{\tau}, u) = -\sum_K \int_K u \nabla \cdot \boldsymbol{\tau} \, \mathrm{d}\mathbf{x} + \sum_{\Gamma_{\mathrm{INP}}} \int_e \{u\}[\![\boldsymbol{\tau}]\!] \cdot \mathbf{n}_e \, \mathrm{d}s, \tag{14a}$$

$$b_h(\boldsymbol{\sigma}, \boldsymbol{\tau}) = \int_\Omega \boldsymbol{\sigma} \cdot \boldsymbol{\tau} \, \mathrm{d}\mathbf{x}, \tag{14b}$$

$$e_h(u,v) = \sum_{\Gamma_{\mathrm{IDP}}} \int_e \alpha [\![u]\!][\![v]\!] \, \mathrm{d}s, \tag{14c}$$

$$g_h(\boldsymbol{\tau}) = -\int_{\partial\Omega_{\mathrm{D}}} g_{\mathrm{D}} \boldsymbol{\tau} \cdot \mathbf{n} \, \mathrm{d}s, \tag{14d}$$

$$f_h(v) = \int_\Omega f v_h \, \mathrm{d}\mathbf{x} + \int_{\partial\Omega_{\mathrm{N}}} g_{\mathrm{N}} v \, \mathrm{d}s + \int_{\partial\Omega_{\mathrm{D}}} \alpha g_{\mathrm{D}} v \, \mathrm{d}s. \tag{14e}$$

Here $e_h(u, v)$ is the penalty (stabilization) term and $\alpha = \eta/h_e$, with η any positive number, and $h_e \equiv \mathrm{diam}(e)$. Since $\eta \ll 1$ and $\eta \gg 1$ yield ill-conditioned matrices, as shown by Castillo [3], moderate values of $\eta(\approx \mathcal{O}(1))$ should be chosen in practice. Note that the original formulation of Bassi and Rebay [32] lacks stabilization, i.e., $e_h(u, v) = 0$.

Remark 3. In the weak imposition of periodic BCs, for the IP and the local DG formulation, ∇u is also assumed to be periodic, so as to yield a symmetric discretization.

Remark 4. Applying the nodal high-order basis (described in Section 3) in Eqs. (13a) and (13b) yields

$$\begin{bmatrix} \mathscr{B} & \mathscr{D}^{\mathrm{T}} \\ \mathscr{D} & \mathscr{E} \end{bmatrix} \begin{bmatrix} \underline{\boldsymbol{\sigma}}_h \\ \underline{u}_h \end{bmatrix} = \begin{bmatrix} \underline{\mathbf{z}}_1 \\ \underline{z}_2 \end{bmatrix}, \tag{15}$$

where $\underline{\mathbf{z}}_1$ and $\underline{z}_2$ represent the given right-hand side and boundary data. Here, a bold matrix consists of d identical blocks. If n_u and $n_{\boldsymbol{\sigma}}$ are the number of degrees of freedom of a component of u_h and $\boldsymbol{\sigma}_h$, respectively, the matrix $\mathscr{B}$ consists of d identical diagonal blocks of size $n_{\boldsymbol{\sigma}} \times n_{\boldsymbol{\sigma}}$ each, corresponding to the mass term, and the matrix $\mathscr{D}$ consists of d blocks of size $n_u \times n_{\boldsymbol{\sigma}}$ each, corresponding to the divergence term. The matrix $\mathscr{E}$ is $n_u \times n_u$, corresponding to the penalty term. After elimination of $\boldsymbol{\sigma}_h$ from the above system, the matrix equation for finding $\underline{u}_h$ becomes

$$(-\mathscr{D}\mathscr{B}^{-1}\mathscr{D}^{\mathrm{T}} + \mathscr{E})\underline{u}_h = \underline{z}, \tag{16}$$

where $\underline{z}$ corresponds to the given right-hand side and boundary data.

Remark 5. While the IP method offers a compact stencil size (Fig. 1a), the local DG method yields an extended stencil size (Fig. 1b). The larger stencil size leads to higher computations and communications per global stiffness matrix construction and global stiffness matrix-vector product.

2.4. DG formulation of the unsteady Stokes operator

Following [20,19], we first give the DG discretization of the system (2). The discontinuous approximations $\mathbf{u}_h$ and p_h are defined by requiring that

$$A_h(\mathbf{u}_h, \mathbf{v}_h) + B_h(\mathbf{u}_h, \mathbf{v}_h) + D_h(\mathbf{v}_h, p_h) = F_h(\mathbf{v}_h) \quad \forall \mathbf{v}_h \in \mathscr{V}_k^d, \tag{17a}$$

$$D_h(\mathbf{u}_h, q_h) = G_h(q_h) \quad \forall q_h \in \mathscr{V}_k/\mathscr{V}_{k-1}, \tag{17b}$$

where

$$A_h(\mathbf{u}, \mathbf{v}) = \sum_K \int_K \frac{1}{Re}\nabla\mathbf{u} : \nabla\mathbf{v}\,\mathrm{d}\mathbf{x} - \sum_{\Gamma_{\mathrm{IDP}}} \int_e \frac{1}{Re}[\mathbf{n}_e \cdot \{\nabla\mathbf{u}\} \cdot [\![\mathbf{v}]\!] + \mathbf{n}_e \cdot \{\nabla\mathbf{v}\} \cdot [\![\mathbf{u}]\!]]\,\mathrm{d}s + \sum_{\Gamma_{\mathrm{IDP}}} \int_e \frac{\mu}{Re}[\![\mathbf{u}]\!] \cdot [\![\mathbf{v}]\!]\,\mathrm{d}s, \tag{18a}$$

$$B_h(\mathbf{u}, \mathbf{v}) = \sum_K \int_K \frac{\beta_0}{\Delta t}\mathbf{u} \cdot \mathbf{v}\,\mathrm{d}\mathbf{x}, \tag{18b}$$

$$D_h(\mathbf{v}, q) = -\sum_K \int_K q\nabla \cdot \mathbf{v}\,\mathrm{d}\mathbf{x} + \sum_{\Gamma_{\mathrm{IDP}}} \int_e \{q\}[\![\mathbf{v}]\!] \cdot \mathbf{n}_e\,\mathrm{d}s, \tag{18c}$$

$$F_h(\mathbf{v}) = \int_\Omega \mathbf{f} \cdot \mathbf{v}\,\mathrm{d}\mathbf{x} + \int_{\Omega_{\mathrm{D}}} \frac{1}{Re}[-\mathbf{g}_{\mathrm{D}} \cdot \nabla\mathbf{v} \cdot \mathbf{n} + \mu\mathbf{g}_{\mathrm{D}} \cdot \mathbf{v}]\,\mathrm{d}s, \tag{18d}$$

$$G_h(q) = \int_{\Omega_{\mathrm{D}}} q\mathbf{g}_{\mathrm{D}} \cdot \mathbf{n}\,\mathrm{d}s. \tag{18e}$$

For the viscous term, the IP method is used because of its simplicity and compact stencil size. The discretization of the two operators ∇p and $\nabla \cdot \mathbf{u}$ are similar to that of ∇u and $\nabla \cdot \boldsymbol{\sigma}$ in Eqs. (13a) and (13b). The only difference is that the roles of the Dirichlet and outflow boundary conditions are switched in the surface integrals of $D_h(\mathbf{v}, q)$ and $d_h(u, \boldsymbol{\tau})$.

Remark 6. Analogous to Remark 1, the terms $\nabla\mathbf{u}:\nabla\mathbf{v}$ and $\mathbf{n}_e \cdot \{\nabla\mathbf{u}\} \cdot [\![\mathbf{v}]\!]$ in Eq. (18a) are evaluated as:

$$\nabla\mathbf{u} : \nabla\mathbf{v} := \frac{\partial u_i}{\partial x_j}\frac{\partial v_i}{\partial x_j} \quad i,j = 1,\ldots,d, \tag{19a}$$

$$\mathbf{n}_e \cdot \{\nabla\mathbf{u}\} \cdot [\![\mathbf{v}]\!] := n_{ej}\left\{\frac{\partial u_i}{\partial x_j}\right\}[\![v_i]\!] \quad i,j = 1,\ldots,d. \tag{19b}$$

Now, let the matrix form of the discretized Stokes system be

$$\begin{bmatrix} \mathbf{H} & \mathbf{D}^{\mathrm{T}} \\ \mathbf{D} & 0 \end{bmatrix}\begin{bmatrix} \underline{\mathbf{u}}^{n+1} \\ \underline{p}^{n+1} \end{bmatrix} = \begin{bmatrix} \underline{\mathbf{f}}^{n+1} \\ \underline{g}^{n+1} \end{bmatrix}, \tag{20}$$

where $\mathbf{H} = (1/Re)\mathbf{A} + (\beta_0/\Delta t)\ \mathbf{B}$ with $\mathbf{A}$ and $\mathbf{B}$ denoting the Laplacian and block diagonal mass matrices, respectively. The descriptions of the matrices are similar to those in Eq. (15).

Applying an LU factorization procedure to the above system and writing the system for the pressure increment variable $\underline{p}^{n+1} - \underline{p}^{n}$, instead of $\underline{p}^{n+1}$, yields

$$\begin{bmatrix} \mathbf{H} & \mathbf{0} \\ \mathbf{D} & -\mathbf{D}\mathbf{H}^{-1}\mathbf{D}^{\mathrm{T}} \end{bmatrix}\begin{bmatrix} \mathbf{I} & \mathbf{H}^{-1}\mathbf{D}^{\mathrm{T}} \\ \mathbf{0} & I \end{bmatrix}\begin{bmatrix} \underline{\mathbf{u}}^{n+1} \\ \underline{p}^{n+1} - \underline{p}^{n} \end{bmatrix} = \begin{bmatrix} \underline{\mathbf{f}}^{n+1} \\ \underline{g}^{n+1} \end{bmatrix} + \begin{bmatrix} -\mathbf{D}^{\mathrm{T}}\underline{p}^{n} \\ 0 \end{bmatrix}.$$

By introducing the auxiliary vector $\underline{\widetilde{\mathbf{u}}}^{n+1}$, the solution procedure for the above system can be written in three steps as follows:

$$\begin{aligned} &1.\ \mathbf{H}\underline{\widetilde{\mathbf{u}}}^{n+1} = \underline{\mathbf{f}}^{n+1} - \mathbf{D}^{\mathrm{T}}\underline{p}^{n}, \\ &2.\ (-\mathbf{D}\mathbf{H}^{-1}\mathbf{D}^{\mathrm{T}})(\underline{p}^{n+1} - \underline{p}^{n}) = -\mathbf{D}\underline{\widetilde{\mathbf{u}}}^{n+1} + \underline{g}^{n+1}, \\ &3.\ \underline{\mathbf{u}}^{n+1} = \underline{\widetilde{\mathbf{u}}}^{n+1} - \mathbf{H}^{-1}\mathbf{D}^{\mathrm{T}}(\underline{p}^{n+1} - \underline{p}^{n}). \end{aligned} \tag{21}$$

The first and second steps involve linear system solves, and the preferred approach is an iterative method. For the pressure increment solution, step 2, each iteration requires extra inner iterations associated with the inversion of matrix $\mathbf{H}$. The inner iterations are avoided by replacing $\mathbf{H}^{-1}$ with the computationally more efficient matrix $\mathbf{H}_{\mathrm{I}} = (\Delta t/\beta_0)\mathbf{B}^{-1}$, where $\mathbf{B}$ is block diagonal, and easily invertible. As shown in [30], this choice leads to a second-order accurate approximation in time. Replacing $\mathbf{H}^{-1}$ with $\mathbf{H}_{\mathrm{I}}$ in (21), we obtain the approximate split solution procedure

$$\begin{aligned} &1.\ \mathbf{H}\underline{\widetilde{\mathbf{u}}}^{n+1} = \underline{\mathbf{f}}^{n+1} - \mathbf{D}^{\mathrm{T}}\underline{\widehat{p}}^{n}, \\ &2.\ (-\mathbf{D}\mathbf{H}_{\mathrm{I}}\mathbf{D}^{\mathrm{T}})(\underline{\widehat{p}}^{n+1} - \underline{\widehat{p}}^{n}) = -\mathbf{D}\underline{\widetilde{\mathbf{u}}}^{n+1} + \underline{g}^{n+1}, \\ &3.\ \underline{\widehat{\mathbf{u}}}^{n+1} = \underline{\widetilde{\mathbf{u}}}^{n+1} - \mathbf{H}_{\mathrm{I}}\mathbf{D}^{\mathrm{T}}(\underline{\widehat{p}}^{n+1} - \underline{\widehat{p}}^{n}) \end{aligned} \tag{22}$$

where $\underline{\widehat{\mathbf{u}}}$ and $\underline{\widehat{p}}$ are the approximations to $\underline{\mathbf{u}}$ and $\underline{p}$, respectively.

The first and the second steps are solved iteratively by using the conjugate gradient method. Since $Re/\Delta t \gg 1$, the Helmholtz solves are effectively preconditioned by the block diagonal mass matrix, leading to a small number of iterations typically of $\mathcal{O}(1)$. On the other hand, the pressure solve requires a more sophisticated and more expensive preconditioner, and thus it is the dominant computation in terms of cost. Moreover, the cost of a single iteration without preconditioning is also higher for the pressure case, since the pressure operator $(-\mathbf{D}\mathbf{H}_{\mathrm{I}}\mathbf{D}^{\mathrm{T}})$ has an extended stencil similar to Fig. 1b. To alleviate this cost, one may attempt to reduce the pressure stencil size. In the DG setting, this strategy appears plausible.

Careful inspection of the pressure operator $(-\mathbf{D}\mathbf{H}_{\mathrm{I}}\mathbf{D}^{\mathrm{T}})$ reveals that this operator is identical (to within a multiplicative constant) to the operator in Eq. (16) with $\mathscr{E} = 0$, except that the roles of Dirichlet and Neumann

BCs are switched in $\mathbf{D}$ and $\mathscr{D}$ (compare the definition of the divergence in Eqs. (18c) and (14a)). In other words, $(-\mathbf{D}\mathbf{H}_\mathrm{I}\mathbf{D}^\mathrm{T})$ results from the application of the local DG method (with zero stabilization) to a Laplacian with the following BCs:

$$\nabla v \cdot \mathbf{n} = 0 \quad \text{on } \partial\Omega_\mathrm{D} \tag{23a}$$

$$v = 0 \quad \text{on } \partial\Omega_\mathrm{N} \tag{23b}$$

$$v(\mathbf{x}) = v(\mathbf{x}') \quad \mathbf{x}, \mathbf{x}' \in \partial\Omega_\mathrm{P}. \tag{23c}$$

Having realized this, we propose to replace the pressure operator $(-\mathbf{D}\mathbf{H}_\mathrm{I}\mathbf{D}^\mathrm{T})$ with the operator arising from the IP discretization of the (negative) Laplacian with the above BCs:

$$\mathscr{A}_h(\mathbf{u},\mathbf{v}) = \sum_K \int_K \nabla\mathbf{u} : \nabla\mathbf{v}\,\mathrm{d}\mathbf{x} - \sum_{\Gamma_\mathrm{INP}} \int_e [\mathbf{n}_e \cdot \{\nabla\mathbf{u}\} \cdot [\![\mathbf{v}]\!] + \mathbf{n}_e \cdot \{\nabla\mathbf{v}\} \cdot [\![\mathbf{u}]\!]]\,\mathrm{d}s + \sum_{\Gamma_\mathrm{INP}} \int_e \mu[\![\mathbf{u}]\!] \cdot [\![\mathbf{v}]\!]\,\mathrm{d}s. \tag{24}$$

The justification is that the IP method and the local DG method are asymptotically similar for stability, boundedness, and the optimal rate of convergence as shown by Arnold et al. [2] in a unified analysis of the DG methods for elliptic problems. Note that since the replacement is applied at the algebraic level, no unphysical BCs have been introduced. Denoting the matrix form of the operator (24) with $\mathscr{A}$ and then replacing $(-\mathbf{D}\mathbf{H}_\mathrm{I}\mathbf{D}^\mathrm{T})$ with $\mathscr{A}$ in (22) yields

$$\begin{aligned}
&1.\ \mathbf{H}\widetilde{\underline{\mathbf{u}}}^{n+1} = \underline{\mathbf{f}}^{n+1} - \mathbf{D}^\mathrm{T}\widehat{\underline{p}}^{n},\\
&2.\ \frac{\Delta t}{\beta_0}\mathscr{A}(\widehat{\underline{p}}^{n+1} - \widehat{\underline{p}}^{n}) = \mathbf{D}\widetilde{\underline{\mathbf{u}}}^{n+1} - \underline{g}^{n+1},\\
&3.\ \widehat{\underline{\mathbf{u}}}^{n+1} = \widetilde{\underline{\mathbf{u}}}^{n+1} - \mathbf{H}_I\mathbf{D}^\mathrm{T}(\widehat{\underline{p}}^{n+1} - \widehat{\underline{p}}^{n}).
\end{aligned} \tag{25}$$

Using the solution procedure (25) instead of (22) simplifies the whole method, in the sense that we use the same scheme (the IP method) for the velocity and pressure operators. Moreover, it enhances the overall efficiency of the scheme by reducing the cost per iteration of a pressure solve.

3. Implementation

For the approximating polynomial space for the velocity or pressure restricted to each element, $P_k(K)$, we choose a high-order nodal basis consisting of Lagrange interpolating polynomials defined on a reference simplex and the nodal set introduced in [9,10], in two and three space dimensions. More specifically, let $\Xi = \{\boldsymbol{\xi}_i \in O\colon 0 \leqslant i \leqslant N\}$ denote the nodal set, where O is the reference element, and $N+1 = (k+1)(k+2)/2$ or $N+1 = (k+1)(k+2)(k+3)/6$ for triangular or tetrahedral elements, respectively. Then, the nodal basis is a set of the Lagrange interpolating polynomials with

$$L_i(\boldsymbol{\xi}_j) = \delta_{ij}, \quad \forall i,j = 0,\ldots,N,$$

where δ_{ij} denotes the Kronecker delta. The interpolation representation of a function $f \in P_k(K)$ is

$$f(\boldsymbol{\xi}) = \sum_{j=0}^{N} f(\boldsymbol{\xi}_j)L_j(\boldsymbol{\xi}). \tag{26}$$

The Lagrange polynomials are the solution of the following system:

$$\sum_{j=0}^{N} b_i(\boldsymbol{\xi}_j)L_j(\boldsymbol{\xi}) = b_i(\boldsymbol{\xi}), \quad \forall i = 0,\ldots,N \tag{27}$$

with $\mathscr{J} = \{b_i(\boldsymbol{\xi}) | \boldsymbol{\xi} \in O, 0 \leqslant i \leqslant N\}$ being an orthonormal basis consisting of multivariate analogues of the Jacobi polynomials (see [41,17,6]).

We follow [16,11] for the derivative and inner-product calculations. Below, we describe quadrature for the nonlinear term evaluation.

3.1. Quadrature for the nonlinear term

The nonlinear term is evaluated by using quadrature of sufficiently high order to ensure accurate and stable integration. Specifically, to eliminate any possible quadrature effects in the following tests, for $k \leqslant 6$, a quadrature order $q = 3k$ has been used, while for $k = 7$, and 8, $q = 19$ has been used. Let $R = \{\boldsymbol{\zeta}_i \in O: 0 \leqslant i \leqslant M\}$ denote a set of $(M+1)$ quadrature points and $W = \{w_i | : 0 \leqslant i \leqslant M\}$ be the corresponding set of quadrature weights. Then, the numerical integration of the first term on the right-hand side of Eq. (5) is carried out as

$$\int_K \underline{\underline{g}} \cdot \nabla \cdot \mathbf{v}_h \, \mathrm{d}\mathbf{x} \approx \sum_{i=0}^{M} J_K w_i \underline{\underline{g}}(\boldsymbol{\zeta}_i) \cdot \nabla \cdot \mathbf{v}_h(\boldsymbol{\zeta}_i), \tag{28}$$

where

$$\underline{\underline{g}}(\boldsymbol{\zeta}_i) = \sum_{j=0}^{N} L_j(\boldsymbol{\zeta}_i) \underline{\underline{g}}(\boldsymbol{\xi}_j), \tag{29a}$$

$$\nabla \cdot \mathbf{v}_h(\boldsymbol{\zeta}_i) = \sum_{j=0}^{N} L_j(\boldsymbol{\zeta}_i) \nabla \cdot \mathbf{v}_h(\boldsymbol{\xi}_j) \tag{29b}$$

and J_K is the Jacobian of the affine map between O and K. The numerical integration of the surface integral in Eq. (5) is carried out in a similar manner. For the following tests, we have used R and W reported in [40].

4. Verification

We have programmed a two-dimensional version of the above scheme in C++ using the algorithm oriented mesh database (AOMD) [39] and the portable, extensible toolkit for scientific computing (PETSc) [36,37].

Below, we present some benchmarking tests to verify the accuracy of the proposed method. We will solve an unsteady Stokes problem to confirm temporal convergence and will then examine the spatial accuracy and the stability of the scheme using equal- and mixed-order methods for the Navier–Stokes equations for three tests: the Taylor vortex problem, the Orr–Sommerfeld plane channel stability problem and flow past a square cylinder at $Re = 100$.

4.1. Temporal error test

Using a second-order backward differentiation temporal discretization and our proposed DG scheme, we solved the unsteady Stokes problem, (Eqs. (1a) and (1b) without the nonlinear term and the body force, $Re = 1.0$) having the exact solution

$$\mathbf{u} = (\sin(x)(a\sin(ay) - \cos(a)\sinh(y))\mathbf{i} + \cos(x)(\cos(ay) + \cos(a)\cosh(y))\mathbf{j})\exp(-\lambda t), \tag{30a}$$

$$p = \lambda \cos(a)\cos(x)\sinh(y)\exp(-\lambda t), \tag{30b}$$

where $a = 2.883356$ and $\lambda = 9.313739$ [15]. The computational domain was $\Omega = [-1,1]^2$, and Dirichlet BCs and initial conditions were based on the above exact solution. We used equal interpolation orders of 8 for the velocity and pressure, and the mesh consisted of 72 semi-structured triangles (similar to that in Fig. 3a). The following results were essentially identical to those obtained using a lower interpolation order $k = 7$, confirming that spatial errors were dominated by the temporal errors, as required for a temporal convergence study. We measured the errors in the L^2 norms:

$$\|e_u\| = \frac{\|\mathbf{u}^n - \mathbf{u}_h(n\Delta t)\|_{L^2(\Omega)}}{\|\mathbf{u}^n\|_{L^2(\Omega)}}, \tag{31a}$$

$$\|e_p\| = \frac{\|p^n - p_h(n\Delta t)\|_{L^2(\Omega)}}{\|p^n\|_{L^2(\Omega)}}. \tag{31b}$$

The L^2 norms were calculated based on the nodal values. For a total integration time $T = 0.1$ during which the initial solution decayed approximately threefold, the results are depicted in Fig. 2. The slope of the best linear fit for the velocity is 1.99, verifying the expected convergence rate. For the pressure the slope is 1.83, slightly smaller than the expected theoretical value.

4.2. Taylor vortex problem

For the first spatial error test, we solved the unsteady Navier–Stokes equations on the square domain $[-1,1]^2$ with $Re = 100$, Dirichlet BCs and initial conditions based on the exact solution:

$$\mathbf{u} = (-\cos(\pi x)\sin(\pi y)\mathbf{i} + \sin(\pi x)\cos(\pi y)\mathbf{j})\exp\left(\frac{-2\pi^2 t}{Re}\right), \tag{32a}$$

$$p = -\frac{\cos(2\pi x) + \cos(2\pi y)}{4}\exp\left(\frac{-4\pi^2 t}{Re}\right). \tag{32b}$$

We carried out convergence studies for both successive approximation order enrichment (p-convergence) and successive mesh refinements (h-convergence).

For the p-convergence, two meshes were used: a semi-structured mesh (Fig. 3a) and a fully unstructured one (Fig. 3b). The time step size $\Delta t = 10^{-4}$ was chosen to satisfy the CFL condition and to ensure that the dominant error was the spatial error. (This was verified by choosing a larger time step $\Delta t = 2 \times 10^{-4}$, which gave virtually identical results). The relative maximum errors in the calculated velocity and pressure for both equal- and mixed-order methods at $T = 5$ (corresponding to approximately threefold decay of the initial solution) and for a range of polynomial degrees $k = 2,\ldots,6$ are depicted in Figs. 3c and d for the semi-structured and unstructured meshes, respectively. Several points about the results are notable. First, an exponential rate of convergence was obtained with respect to the approximating polynomial degree for both velocity and pressure and for both mixed- and equal-order formulations. Second, for the semi-structured mesh, equal- and mixed-order methods led to results with very similar accuracy. On the other hand, for the unstructured mesh, using $P_k - P_k$ interpolations yielded more accurate results in both velocity and pressure than those resulting from $P_k - P_{k-1}$ interpolations.

To test the h-convergence, we only used the semi-structured mesh (similar to Fig. 3a). For the same time step size and the total time as the former case, the relative L^2 errors in calculated velocity versus element size for a range of polynomial degrees $k = 4,\ldots,8$ for both $P_k - P_k$ and $P_k - P_{k-1}$ formulations are depicted in Figs. 4a and b, respectively. Figs. 4c and d show the corresponding results of equal- and mixed-order methods for the calculated pressure. Similar to the p-convergence test, $P_k - P_k$ methods led to slightly more accurate

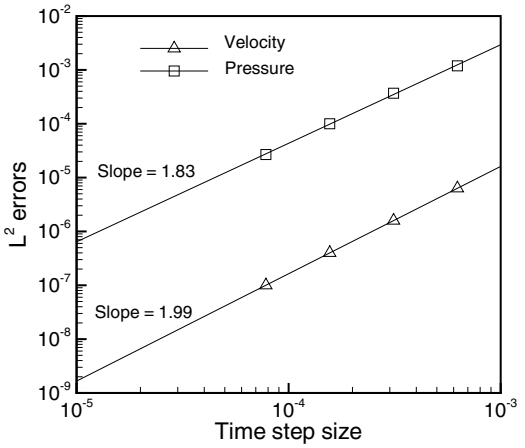

Fig. 2. L^2 norm errors in velocity and pressure calculated based on Eqs. (31a) and (31b) vs. the time step size in solving an unsteady Stokes problem with the DG method described in Section 2, a semi-structured mesh consisting of 72 triangles (Fig. 3a), and equal interpolation orders of 8. For each data set, the best linear fit and its slope are also shown.

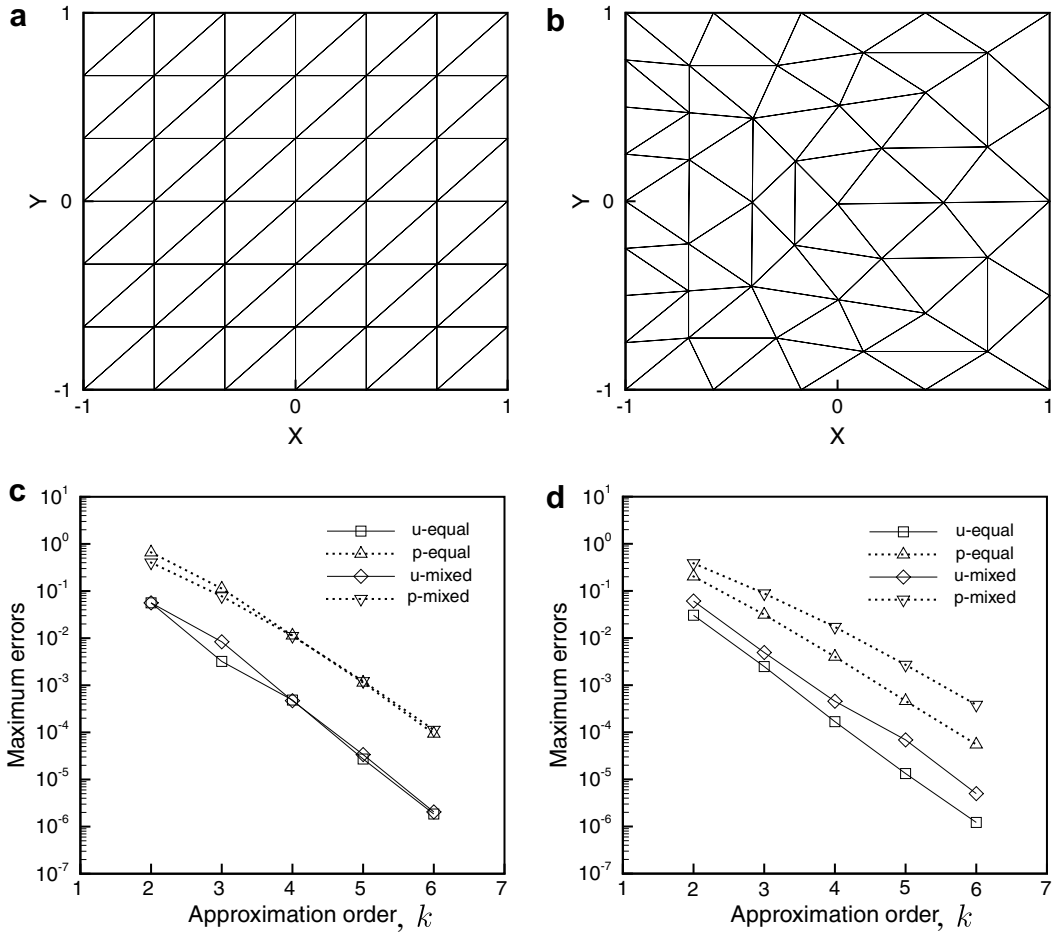

Fig. 3. (a) Computational domain used for tests partitioned into 72 semi-structured triangular elements; (b) the same domain partitioned into 72 unstructured triangular elements generated using Gmsh software [8]; (c) and (d) maximum errors in calculated velocity and pressure vs. approximating polynomial degrees in solving the Taylor vortex problem using meshes in Figs. 3a and b, respectively. In the legend, "*u*-equal" refers to the error in velocity for equal order interpolation. "*p*-equal" is the corresponding error in the pressure. "mixed" refers to the $P_k - P_{k-1}$ formulation.

results than those of $P_k - P_{k-1}$ for most cases. Moreover, we observed optimal rate of convergence in velocity for both $P_k - P_k$ and $P_k - P_{k-1}$ formulations. For the pressure, on the other hand, optimal rates of convergence were only obtained for the mixed-order method, as expected. The equal-order method led to suboptimal rates for the pressure.

Note that although both equal- and mixed-order methods led to stable results for this simple problem, the mixed-order method leads to unstable results for more challenging (high Reynolds number) tests such as Orr–Sommerfeld stability problem as shown below.

4.3. Orr–Sommerfeld stability problem

We further investigated the spatial accuracy as well as the stability of our proposed method by solving the Orr–Sommerfeld stability problem. This is a suitable benchmarking test in that it is an unforced time-dependent solution of the Navier–Stokes equations for which an accurate solution is available from linear stability analysis [7]. The geometry was a two-dimensional channel $[x = 0, x = 2\pi] \times [y = -1, y = 1]$. Dirichlet BCs were imposed in the spanwise direction (at $y = -1$ and $y = 1$) and periodic BCs were applied in the streamwise direction (at $x = 0$ and $x = 2\pi$). The initial conditions were

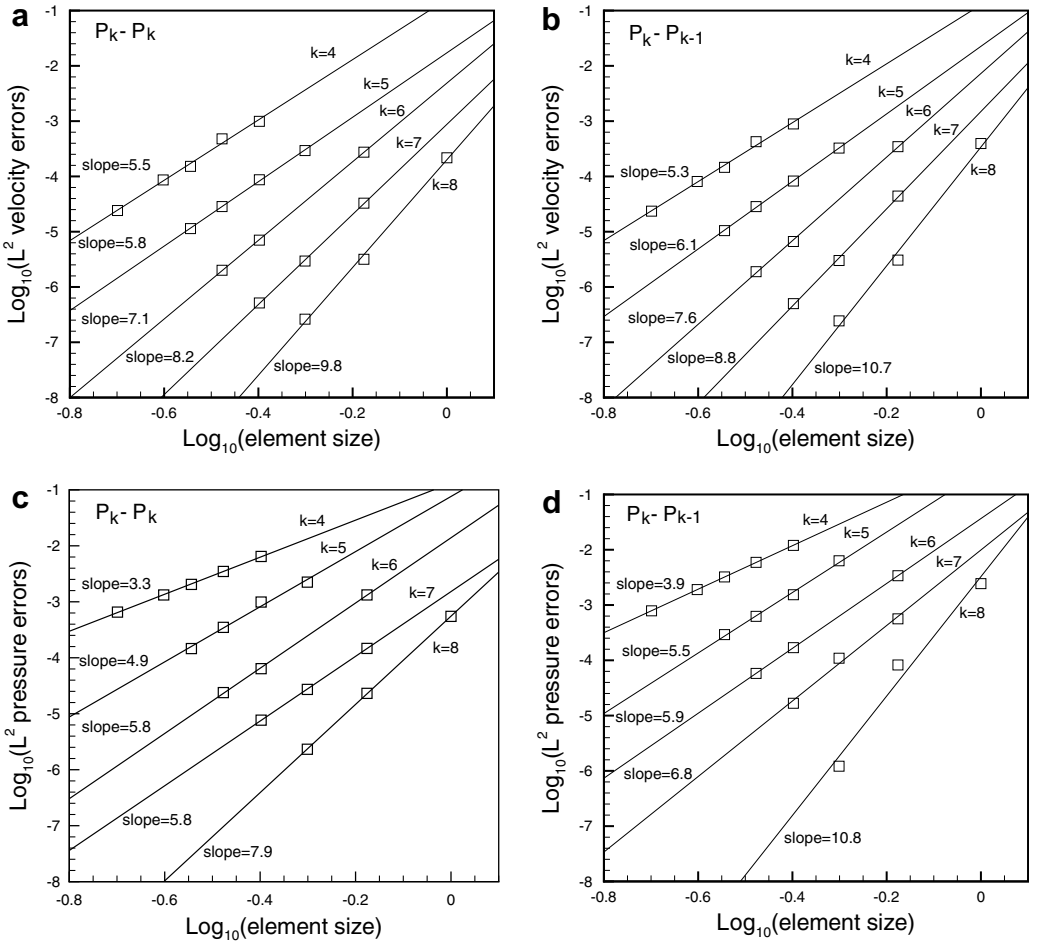

Fig. 4. (a) and (b) L^2 velocity errors vs. element size of semi-structured meshes for interpolation order $k = 4,\ldots,8$, in solving the Taylor vortex problem using equal- and mixed-order methods, respectively. (c) and (d) The corresponding equal- and mixed-order data for the pressure. For each data set, the best linear fit and its slope are also shown.

$$u = 1 - y^2 + \epsilon\hat{u}, \tag{33a}$$

$$v = \epsilon\hat{v}, \tag{33b}$$

where (u,v) represent the velocity components in the (x, y) directions. Here $(\hat{u}, \hat{v})$ (Tollmien–Schlichting waves, T–S waves) correspond to the only unstable eigensolution of the Orr–Sommerfeld equation with wave number unity at $Re = 7500$. We set ϵ to 10^{-4}. More details of this test can be found in [4].

According to linear stability theory, the perturbation energy

$$E(t) = \int_0^{2\pi}\int_{-1}^{1}[(1 - y^2 - u)^2 + v^2]\,\mathrm{d}y\,\mathrm{d}x \tag{34}$$

should grow as $e^{2\omega_i t}$, where $\omega_i = 0.002234976$ is the growth rate.

For both $P_k - P_k$ and $P_k - P_{k-1}$ formulations with $k = 6$ and 8 and for a semi-structured mesh consisting of 128 triangles, and $\Delta t = 10^{-3}$ (smaller than Δt arising from the CFL condition) we plot the computed perturbation energy and its growth rate versus the normalized time (T/T_0) in Figs. 5a and b, respectively. In the same figures, the corresponding results from linear stability theory are also depicted. In the $P_k - P_k$ formulation for $k = 6$, we observed some dissipation (Fig. 5a); however, increasing the resolution to $k = 8$ led to perturbation energy growth almost identical to the theoretical one. We also calculated the error in the growth rate at $T = 60$. For $k = 6$, 7, and 8, we obtained growth rates $\omega = 0.001936496$, 0.002156142, and 0.002234850.

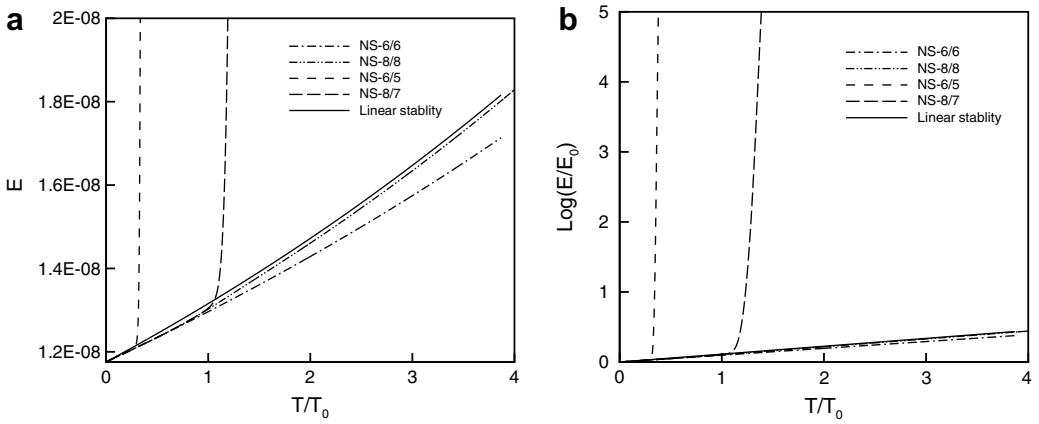

Fig. 5. (a) Perturbation energy vs. normalized time in solving the Orr–Sommerfeld problem for both equal- and mixed-order methods; (b) the same test, showing the energy growth rate. The symbols NS-6/6 and NS-6/5 (NS-8/8 and NS-8/7) represent the computed Navier–Stokes solutions using $P_k - P_k$ and $P_k - P_{k-1}$ with $k = 6$ ($k = 8$). Scaling parameters are $E_0 = E(t = 0)$, and $T_0 = 25.1437$, the time taken for a T–S wave to travel the channel length, 2π.

The corresponding errors calculated as $e_g = |\omega - \omega_i|/\omega_i$ were $e_g = 1.34e-1, 3.53e-2$, and $5.62e-5$. A spectral rate of convergence was clearly obtained.

In the $P_k - P_{k-1}$ formulation, however, we observed a totally different behavior. For $k = 6$, we observed perturbation energy blowup at $T \approx 0.3T_0$. As shown in Fig. 5b, this unphysical behavior was characterized by orders-of-magnitude increase in the energy growth rate in a very short period of time. When the resolution was increased to $k = 8$, the same blowup occurred, but at a later time $T/T_0 \approx 1$, making the diagnosis of this instability more difficult.

The source of this instability is similar to that of the instability occurring in the $Q_k - Q_{k-2}$ spectral element solution scheme for the Navier–Stokes equations reported in [42]. For the same Orr–Sommerfeld problem, Wilhelm and Kleiser [42] observed unphysical perturbation energy growth when the divergence form of the nonlinear term was discretized. Through an eigenvalue analysis of the full discretized linear system, they found eigenvalues with positive real parts (see Fig. 8 in [42]). Furthermore, they showed that the divergence of the velocity field grew exponentially at those points for which the divergence-free constraint was not enforced (see Figs. 4 and 5 in [42]). For our mixed-order DG formulation the situation is similar. Since the velocity and pressure nodes are different, there is a chance of unphysical instability. For the equal-order method, however, velocity and pressure nodes are identical; thus, the formulation is stable. The rigorous analysis of the stability of the method will be addressed in a forthcoming paper.

4.4. Flow past a square cylinder

As a final test, we examine the spatial accuracy of our method by simulating vortex shedding in flow past a square cylinder at $Re = 100$, based on the unit inflow velocity and the square edge length. The geometry consisted of a unit square located in a rectangular domain with vertices $(-16, -22)$, $(25, -22)$, $(-16, 22)$, and $(25, 22)$, where the origin was placed in the center of the cylinder (see Fig. 6, left). This yields a blockage ratio $B = 2.3\%$. This geometry is identical to the geometry used in [27] and is chosen because it leads to geometry-independent results as shown in [28]. With flow in the positive x-direction, we imposed the following boundary conditions: zero Dirichlet BCs on the square, $\mathbf{u} = (1, 0)$ on the inlet and side walls and outflow BCs at the outlet. The mesh consists of 1706 triangles concentrated on the cylinder to resolve the large gradient of vorticity associated with the sharp corners (Fig. 6). We used the $P_k - P_k$ method with $k = 4$ and $\Delta t = 10^{-3}$.

An instantaneous view of the calculated vorticity contours are shown in Fig. 7, demonstrating the von-Karman vortex downstream of the cylinder. For comparison with available data in the literature, we calculated the Strouhal number $St = fD/u$, where f is the frequency of the vortex shedding, $u = 1$ the inflow velocity and $D = 1$ the edge length of the cylinder. The frequency was obtained from spectral analysis of the lift coefficient

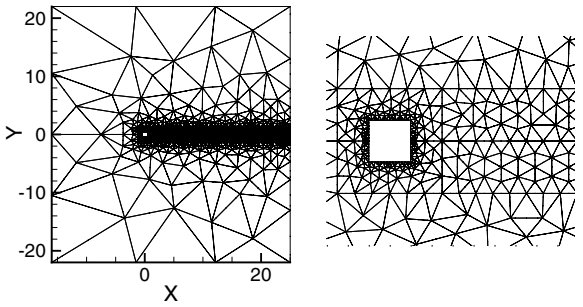

Fig. 6. The mesh for flow past square cylinder generated using Gmsh software [8]. Entire domain with 1706 triangles (left), and zoom-in view near the cylinder (right).

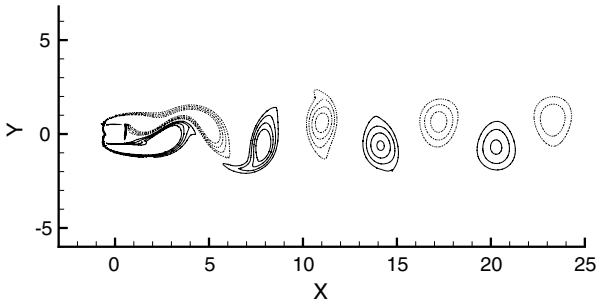

Fig. 7. Snapshot of vorticity contours at $Re = 100$. Solid and dashed lines denote positive and negative vorticity levels in $[-1,1]$, respectively.

Table 1
Comparison of Strouhal number for vortex shedding in flow over a square cylinder at $Re = 100$

Approach	St
Okajima [34, experimental], $B = 0\%$	0.141–0.145
Darekar and Sherwin [27], $B = 2.3\%$	0.145
Present, $B = 2.3\%$	0.145

B is the blockage ratio.

sampled over the time span of $t = 20$ dimensionless times, D/u. Our results, along with experimental data of Okajima [34] and the computational result of Darekar and Sherwin [27], are listed in Table 1. The latter was obtained using a spectral element Navier–Stokes solver with 1502 triangular elements of order $k = 6$. The total number of unknowns of this resolution was almost identical to that of the lower resolution (1706 triangles of order $k = 4$) used in our DG simulation. As is clear from the table, we obtained excellent agreement with both experimental and computational data.

5. Conclusions

We have introduced a simple and efficient method for the numerical solution of the unsteady incompressible Navier–Stokes equations in convection-dominated flow regimes. The method is based on nodal high-order discontinuous Galerkin methods on triangular and tetrahedral meshes and a second order approximate algebraic splitting method. The scheme yields compact stencil sizes for the nonlinear term, and velocity and pressure operators well suited for large-scale parallel computations.

We have verified the temporal and spatial performance of the method on several benchmarking problems. We obtained second-order temporal convergence and spectral spatial convergence, as expected. On the challenging Orr–Sommerfeld test problem, we observed that equal-order polynomial approximations of the velocity and pressure led to a stable solution, while the mixed-order method yielded an unphysical instability. The

equal-order method also performed well in simulating vortex shedding in flow past square cylinder at $Re = 100$.

Several aspects of our implementation can be improved to achieve higher efficiency. First, employing non-conforming mesh adaptation close to the Dirichlet boundaries can significantly reduce the required global degrees of freedom for a given accuracy. Second, efficient preconditioning for the Poisson pressure equation should be devised. The class of optimal two-level overlapping Schwarz preconditioners for the p-version finite element methods recently introduced in [35] can be applicable in the discontinuous Galerkin setting.

Moreover, the cost of core kernels, such as elemental stiffness matrix construction and elemental stiffness matrix–vector multiplication, can be reduced. In our current implementation using a nodal basis, the cost of these operations with respect to the approximating polynomial degree k is $\mathcal{O}(k^{2d})$ floating point operations. This limits the order of approximation to only moderately high values ($k < 12$ for two dimensions and $k < 6$ for three dimensions). Recently, Beuchler and Schöberl [33] introduced a new modal formulation for p-version finite element methods, using integrated Jacobi polynomials. In this formulation, the calculation of the core kernels requires only $\mathcal{O}(k^d)$ floating-point operations. This is significantly lower than those of our current nodal implementation and even the spectral element formulation on tensor product domains (which is $\mathcal{O}(k^{d+1})$). Application of this formulation to discontinuous Galerkin methods is ongoing.

Acknowledgements

The authors thank the anonymous reviewers for their valuable comments. This work was financially supported by the National Sciences and Engineering Council of Canada through operating grant A2191 and by the Mathematical, Information, and Computational Sciences Division subprogram of the Office of Advanced Scientific Computing Research, US Department of Energy, under Contract W-31-109-Eng-38.

References

[1] D. Arnold, An interior penalty finite element method with discontinuous elements, SIAM J. Numer. Anal. 19 (1982) 742–760.
[2] D.N. Arnold, F. Brezzi, B. Cockburn, L.D. Marini, Unified analysis of discontinuous Galerkin methods for elliptic problems, SIAM J. Numer. Anal. 39 (2002) 1749–1779.
[3] P. Castillo, Performance of discontinuous Galerkin methods for elliptic PDEs, SIAM J. Sci. Comput. 24 (2002) 524–547.
[4] C. Canuto, M.Y. Hussaini, A. Quarteroni, T.A. Zang, Spectral Methods in Fluid Dynamics, Springer-Verlag, Heidelberg, 1988.
[5] W. Couzy, Spectral element discretization of the unsteady Navier–Stokes equations and its iterative solution on parallel computers, Thesis No. 1380, École Polytechnique Fédérate de Lausanne, 1995.
[6] M. Dubiner, Spectral methods on triangle and other domains, J. Sci. Comput. 6 (1991) 345–390.
[7] P.F. Fischer, An overlapping Schwarz method for spectral element solution of the incompressible Navier–Stokes equations, J. Comput. Phys. 133 (1997) 84–101.
[8] C. Geuzaine, J.F. Remacle, Gmsh Reference Manual, Edition 1.12. Available from: <http://www.geuz.org.org/gmsh/>, 2003.
[9] J.S. Hesthaven, From electrostatics to almost optimal nodal sets for polynomial interpolation in a simplex, SIAM J. Numer. Anal. 35 (1998) 655–676.
[10] J.S. Hesthaven, C.H. Teng, Stable spectral methods on tetrahedral elements, SIAM J. Sci. Comput. 21 (2000) 2352–2380.
[11] J.S. Hesthaven, T. Warburton, Nodal high-order methods on unstructured grids. I. Time-domain solution of Maxwell's equations, J. Comput. Phys. 181 (2002) 186–221.
[12] G.J. Heywood, R. Rannacher, S. Turek, Artificial boundaries and flux and pressure conditions for the incompressible Navier–Stokes equations, Int. J. Numer. Methods Fluids 22 (1996) 325–352.
[13] G.E. Karniadakis, M. Israeli, S.A. Orszag, High-order splitting methods for the incompressible Navier–Stokes equations, J. Comput. Phys. 97 (1991) 414–443.
[14] G.E. Karniadakis, S.J. Sherwin, Spectral/hp Element Methods for Computational Fluid Dynamics, Oxford Univ. Press, London, 2005.
[15] Y. Maday, A.T. Patera, E.M. Rønquist, An operator-integration-factor splitting method for time-dependent problems: application to incompressibel fluid flow, J. Sci. Comput. 5 (1990) 263–292.
[16] T. Warburton, L.F. Pavarino, J.S. Hesthaven, A pseudo-spectral scheme for the incompressible Navier–Stokes equations using unstructured nodal elements, J. Comput. Phys. 164 (2000) 1–21.
[17] T. Koornwinder, Theory and Application of Special Functions, Academic Press, New York, 1975, pp. 435–495.
[18] D. Schötzau, C. Schwab, A. Toselli, Mixed hp-DGFEM incompressible flows, SIAM J. Numer. Anal. 40 (2003) 2171–2194.

[19] D. Schötzau, C. Schwab, A. Toselli, Mixed hp-DGFEM for incompressible flows. II. Geometric edge meshes, IMA J. Numer. Anal. 24 (2004) 273–308.
[20] P. Hansbo, M.G. Larson, Discontinuous Galerkin methods for incompressible and nearly incompressible elasticity by Nitsche's method, Comput. Methods Appl. Mech. Eng. 191 (2002) 1895–1908.
[21] B. Cockburn, G. Kanschat, D. Schötzau, C. Schwab, Local discontinuous Galerkin methods for the Stokes system, SIAM J. Numer. Anal. 40 (2002) 319–343.
[22] B. Cockburn, G. Kanschat, D. Schötzau, The local discontinuous Galerkin method for the Oseen equations, Math. Comput. 73 (2004) 569–593.
[23] B. Cockburn, G. Kanschat, D. Schötzau, A locally conservative LDG method for the incompressible Navier–Stokes equations, Math. Comput. 74 (2005) 1067–1095.
[24] B. Cockburn, C. Shu, Runge–Kutta discontinuous Galerkin methods for convection-dominated flows, J. Sci. Comput. 16 (2001) 173–261.
[25] B. Cockburn, C. Shu, The local discontinuous Galerkin method for time-dependent convection-diffusion systems, SIAM J. Numer. Anal. 35 (1998) 2440–2463.
[26] T.J.R. Hughes, G. Engel, L. Mazzei, A comparison of discontinuous and continuous Galerkin methods based on error estimates, conservation, robustness and efficiency, in: B. Cockburn, G.E. Karniadakis, C.-W. Shu (Eds.), Discontinuous Galerkin Methods. Theory, Computation and Applications, Lecture Notes in Computational Science and Engineering, vol. 11, Springer-Verlag, 2000, pp. 135–146.
[27] R.M. Darekar, S.J. Sherwin, Flow past a square-section cylinder with a wavy stagnation face, J. Fluid Mech. 426 (2001) 263–295.
[28] D. Barkley, R.D. Henderson, Three-dimensional Floquet stability analysis of the wake of a circular cylinder, J. Fluid Mech. 322 (1996) 215–241.
[29] V. Girault, B. Riviére, M.F. Wheeler, A discontinuous Galerkin method with nonoverlapping domain decomposition for the Stokes and Navier–Stokes problems, Math. Comput. 74 (2005) 53–84.
[30] M.O. Henriksen, J. Holmen, Algebraic splitting for incompressible Navier–Stokes equations, J. Comput. Phys. 175 (2002) 438–453.
[31] K. Shahbazi, An explicit expression for the penalty parameter of the interior penalty method, J. Comput. Phys. 205 (2005) 401–407.
[32] F. Bassi, S. Rebay, A high-order accurate discontinuous finite element method for the numerical solution of the compressible Navier–Stokes equations, J. Comput. Phys. 131 (1997) 267–279.
[33] S. Beuchler, J. Schöberl, New shape functions for triangular p-FEM using integrated Jacobi polynomials, Technical Report 2004-18, Johann Radon Institute for Computational and Applied Mathematics, Linz, Austria. Available from: <http://www.ricam.oeaw.ac.at/publications/reports/04/rep04-18.pdf>.
[34] A. Okajima, Strouhal numbers of rectangular cylinders, J. Fluid Mech. 123 (1982) 379–398.
[35] J. Schöberl, J. Melenk, C. Pechstein, S. Zaglmayr, Additive Schwarz preconditioning for p-version triangular and tetrahedral finite elements. Available from: <http://www.hpfem.jku.at/index.html?/joachim>, 2005.
[36] S. Balay, K. Buschelman, W.D. Gropp, D. Kaushik, M. Knepley, L.C. McInnes, B.F. Smith, H. Zhang, PETSc home page. Available from: http://www.mcs.anl.gov/petsc, 2001.
[37] S. Balay, K. Buschelman, V. Eijkhout, W.D. Gropp, D. Kaushik, M.G. Knepley, L.C. McInnes, B.F. Smith, H. Zhang, PETSc Users Manual, ANL-95/11 - Revision 2.1.5, Argonne National Laboratory, 2004.
[38] J.B. Perot, An analysis of the fractional step method, J. Comput. Phys. 108 (1993) 51–58.
[39] J. Remacle, AOMD home page. Available from: <http://www.scorec.rpi.edu/AOMD/>, 2002.
[40] P. Solin, K. Segeth, I. Dolezel, Higher-order Finite Element Methods, Studies in Advanced Mathematics, Chapman & Hall/CRC, Boca Raton, FL, 2004.
[41] G. Szegö, Orthogonal Polynomials, Am. Math. Soc., Providence, 1939.
[42] D. Wilhelm, L. Kleiser, Stability analysis for different formulations of the nonlinear term in $P_N - P_{N-2}$ spectral element discretizations of the Navier–Stokes equations, J. Comput. Phys. 174 (2001) 306–326.
[43] A.J. Chorin, On the convergence of discrete approximation to the Navier–Stokes equations, Math. Comput. 23 (1969) 341–353.
[44] R. Temam, Une mthode d'approximation de la solution des quations de Navier–Stokes, Bulletin de la Socit Mathmatique de France 96 (1968) 115–152.